

# Measurements and Modeling of the Satellite-to-Indoor Channel for Galileo

F. Pérez-Fontán, B. Sanmartín, *University of Vigo, Spain*. A. Steingass, A. Lehner, J. Selva, *German Aerospace Center, Germany*  
E. Kubista, *Joanneum Research, Graz, Austria*. B. Arbesser-Rastburg, *European Space Agency*

## BIOGRAPHIES

Fernando Pérez-Fontán, was born in Vilagarcía de Arousa, Spain. He received a Telecommunications Engineering degree and a PhD from the Polytechnic University of Madrid in 1982 and 1992. He has been with the Telecommunications Engineering School of Vigo University since 1988, where he currently is a full professor at the Department of Signal Theory and Communications.

Belén Sanmartín, was born in Chantada, Spain. She obtained her Telecommunications Engineering degree from Vigo University in 2001. She has been involved in several GALILEO projects doing deterministic and statistical modeling of the navigation propagation channel.

Alexander Steingass was born in Mettmann, Germany in 1969. He received his Dipl. Ing. diploma in Electrical Engineering in 1997 (University of Ulm, Germany). Since then he has been a research scientist at the German Aerospace Centre DLR - Institute of Communications and Navigation. He has been involved in several projects in the area of satellite navigation and location dependent mobile services. In 2002 he was promoted Dr. Ing. at the University of Essen. <http://www.dlr.de/kn/kn-s/steingass>, [alexander.steingass@dlr.de](mailto:alexander.steingass@dlr.de)

Andreas Lehner was born in Gmunden, Austria in 1973. He received his Diploma Engineer degree in Mechatronics from the University of Linz in 2001. Since then he has been a research scientist at the German Aerospace Centre DLR. <http://www.dlr.de/kn/kn-s/lehner>, [andreas.lehner@dlr.de](mailto:andreas.lehner@dlr.de)

Jesús Selva received the Communications Engineer degree from the Technical University of Valencia (Spain) in 1994, and the Mathematics degree from the UNED University (Spain) in 2000. He currently works at the German Aerospace Centre (DLR) and is about to complete his Ph. D. thesis at the University of Catalonia (Spain).

Erwin Kubista received the Dipl. Ing. degree in Telecommunications and Electronic Engineering from the Technical University of Graz, Austria, in 1985. He is with

Joanneum Research, Graz, where he has been involved with and has lead a number of projects dealing with mobile and fixed satellite wave propagation carried out under ESA and EU contracts.

Bertram Arbesser-Rastburg was born in Austria. He received the Dipl.-Ing. degree in electrical engineering from the Technical University of Graz, Graz, Austria, in 1980. In 1988, he joined the European Space Agency. Since 1989, he has been Head of the Wave Interaction and Propagation Section at the European Space Agency/European Space Technology Center (ESA/ESTEC), Noordwijk, and The Netherlands. His research activities include propagation effects relevant to fixed, mobile, and navigation satellite systems as well as direct and indirect models of microwave interaction with the Earth's surface and the atmosphere for active and passive remote-sensing instruments.

## ABSTRACT

In this paper measurements and modeling results obtained in the course of an European Space Agency, ESA, project (2002-2003) entitled "Navigation signal measurement campaign for critical environments", carried out by JOANNEUM RESEARCH (Austria) with subcontracts to DLR (Germany) and the University of Vigo (Spain), are presented.

During the project, measurements were performed using a high resolution channel sounder on board a helicopter, the objective being the characterization of the satellite-to-indoor channel at frequencies close to those assigned to the future Galileo navigation system. The helicopter was flown around a building where a receiver was located. Different flights were carried out to cover several elevation angles. The receiver was also placed in different locations at different floors within the building so that different penetration conditions could be studied: close to the external walls, corridors, inner rooms, et. al.. Typical measured power-delay profiles, PDPs, are presented and analyzed. In addition, the dynamics of the channel were also studied and characterized.

To complement the study, a modeling activity was carried

out in two directions. For one, the measured environments were studied using a deterministic, ray-tracing based propagation tool to gain further insight on the propagation phenomena. In a second step, a statistical channel model was derived from the measurements.

The statistical model reflects the different time-spreading conditions found in the measurements, which are mainly caused by reflections and diffractions within the building itself and those produced by reflections/diffractions on external buildings. The statistical model also addresses how the arriving contributions reach the receiver in groups or clusters of rays.

## INTRODUCTION

This paper presents an analysis of experimental data for the satellite-to-indoor channel obtained in a measurement campaign carried out by the authors using a helicopter to simulate the navigation satellite and a high resolution wide-band channel sounder. In addition, the paper describes the main issues relative to a deterministic wideband channel model and a statistical model also developed from these measurements. In the last step the measurements were also used to validate the deterministic model.

## MEASUREMENT ANALYSIS

In this section we present an analysis of the results of the satellite-to-indoor channel measurements of 2002-2003. First, we chose a criterion in order to separate the measured snapshots in two sets: (a) snapshots without line-of-sight (LOS) ray and (b) snapshots with LOS ray. Then, we proceeded to calculate the probability of the reflected/diffracted rays falling below a given threshold for the non-LOS set, and performed a statistical analysis of the LOS set. Several issues, like the variation with the elevation angle and the presence of rays from outside the building, are discussed along the analysis.

Throughout this paper we employ the term “delta” to refer to the resulting signal from one ray. This is the usual term in the signal processing field (a Dirac delta).

From the visibility calculation, we selected the snapshots in which there is a direct signal, and we referred the delays to the maximum power epoch. Figure 1 (left) shows the impulse responses in scenario P4 (Table 1) for the 30° elevation circular flight. The snapshots in which there is a direct signal can be easily detected by looking at the maximum power level. In Figure 1 (right), we have retained only the snapshots with sufficient maximum power level. In addition it is noticeable that there is a significant power at negative delays in the snapshots in which there is not a direct signal. This is because the delay reference has been taken at an epoch

corresponding to a reflected/diffracted ray. The maximum snapshot power usually has a 3 dB variation in consecutive snapshots as can be seen in Figure 2.

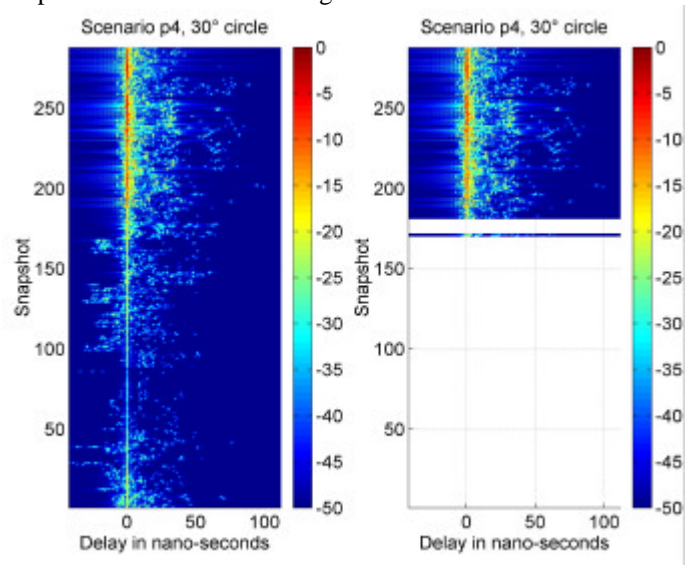


Figure 1. Impulse responses in the 30° elevation circle, scenario P4 (fourth floor), with delays relative to the maximum power epoch. For the plot to the right, we selected a power threshold of 15 dB below the maximum power in all snapshots, and we plotted only those snapshots in which the maximum power is above this threshold.

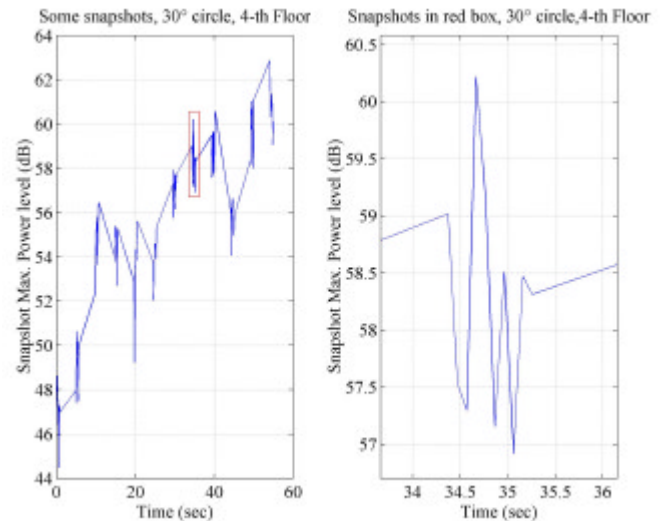


Figure 2. Maximum snapshot power in some snapshots of the 30° elevation circular flight. The red box to the left was zoomed to the right.

In the snapshots without LOS ray, it would be convenient to estimate the probability of a ray falling below a given threshold relative to the LOS level. This probability could be calculated if, for each snapshot, the distance between transmitter and receiver, the antenna gains at the propagation angles, and all the additional losses were known. Unfortunately, it is not possible to determine the antenna

gains for all the propagation angles, given that they depend on the helicopter attitude. Besides, there may be a significant obstruction of the direct signal, even if it is present. The third data column of Table 1 contains the ratio in dB from the average snapshot maximum ray power to the flight maximum ray power. We can see that it can reach high values (up to 14 dB), and this makes it impossible to calculate the link budget from the measurements with LOS propagation. For this reason, we cannot employ the LOS power level at each snapshot as a reference. Instead, we propose to employ the maximum ray power of the whole flight (circular or cross-over).

For a given level  $L$  in dB, let  $\text{Prob}_L$  denote the probability that a delta in a snapshot without direct signal has a level close to the maximum ray power (a difference of less than  $L$  dB). The first and second columns of Table 1 contain the estimations of  $\text{Prob}_{15}$  and  $\text{Prob}_{25}$  for all flights and scenarios. For a given flight, let the index  $k$  run through the snapshots with enough maximum level, (15 dB threshold below the maximum flight ray power), and let  $P_k$  be the maximum power in the  $k$ -th snapshot. The third data column in Table 1 contains

$$S = 10 \log_{10} \left\{ \frac{\max_k \{P_k\}}{\text{mean}\{P_k\}} \right\}.$$

This statistic is a measure of the irregularity of the scenario plus the variations due to other factors, (LOS ray obstruction, gain variation with the helicopter attitude, etc). Whenever there is no direct signal,  $\text{Prob}_{25}$  (or  $\text{Prob}_{15}$ ) takes on a high value. This is because the delta in the  $k$ -th snapshot with power  $P_k$  has been produced by a reflection. Therefore, this power level is similar to any other level in the same snapshot, and  $\text{Prob}_{25}$  is high. Also, for these flights,  $S$  takes on the smallest values (about 6 dB), because  $\max_k \{P_k\}$  is not set by any direct signal.

It is difficult to explain the remaining values due to the various factors involved: helicopter attitude variations, presence of rays from outside the building, and inaccurate LOS reference.

## STATISTICAL MODEL FOR LOS PATHS

In this section, we propose a statistical channel model for the line-of-sight (LOS) paths in which the impulse response is the sum of a direct signal plus some delayed, attenuated and phase shifted replicas. The main parameters of the channel impulse response (delays, amplitudes, number of rays) are considered as random with a probability density function that is estimated from the measured data. The impulse response model is

$$h(t) = \sum_{k=1}^N a_k e^{j\phi_k} d(t - t_k),$$

where

$N$	No. of rays. PDF obtained from measurements.
$a_1$	Direct ray amplitude. (Input parameter in the trial generator.)
$j_1$	Direct ray phase. Uniform in $[0, 2\pi]$ .
$t_1$	Direct ray delay. It is taken equal to zero.
$a_k, k > 1$	Reflection ray amplitude. PDF obtained from measurements.
$j_k, k > 1$	Reflection ray phase. Uniform in $[0, 2\pi]$ .
$t_k, k > 1$	Reflection ray delay. PDF obtained from measurements.

The first step in calculating random trials of the indoor channel is the generation of the **number of rays** in the impulse response. For this task we require the cumulative distribution (cdf) function of this parameter.

Figure 3 shows the estimated cdf in the 30° elevation circular flight for the receiver on the fourth floor. It is visible that there is a jump at the abscissas 29 and 30. This seems due to the fact that the number of rays was limited to 30. We can see that this effect was not produced by the limited dynamic range (35 dB) by looking at Figure 4. In this plot, we find the number of snapshots with a given number of rays inside the dynamic range. We would expect a similar number of snapshots for 29 and 30 rays and for a number of rays close to these values, but there is a sharp increase.

The best solution is to distribute the snapshots with 29 and 30 rays among the abscissas corresponding to a number of rays greater than 28, assigning a similar amount of snapshots to each abscissa, (see Figure 5). In Figure 6, we have recalculated the cdf in Figure 3 by assigning the mean number of snapshots in the last 10 abscissas to the abscissas greater than 28, so that the number of snapshots with more than 28 rays is equal to the number of snapshots with 29 and 30 rays in the uncorrected data. The resulting maximum number of rays is 45. The trial generator employs this cdf.

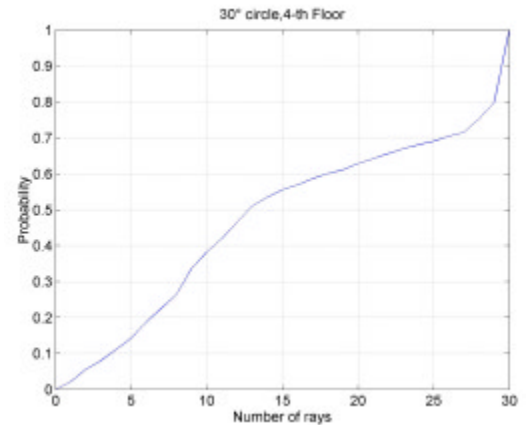


Figure 3. Estimated cumulative distribution functions (cdfs) for the 30° circular flight on the 4<sup>th</sup> floor.

Figures 7-9 show the estimated cdfs in all three floors of the

reflected rays relative powers. Some of the curves are below the probability 1 value for positive power levels, which is not consistent with the normalization relative to the maximum power level in each snapshot. What happens is that the maximum power level cannot be calculated from the data, because there is not a single snapshot with direct ray. Therefore, it was necessary to extrapolate the maximum power level from another flight that contained snapshots with LOS component. Specifically, we chose the snapshots taken on the fourth floor with direct component as a reference. In this extrapolation, it was also necessary to adjust the propagation loss. In Figure 10, we assess the quality of the extrapolation by calculating the cdf of the 10° elevation circular flight with and without extrapolation from the 30° circular flight on the fourth floor. We can see that the maximum probability variation is about 7%.

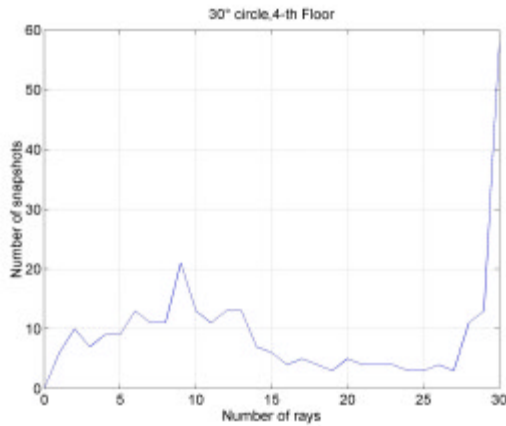


Figure 4. Number of snapshots with a given number of rays inside the dynamic range. Measurements on the fourth floor.

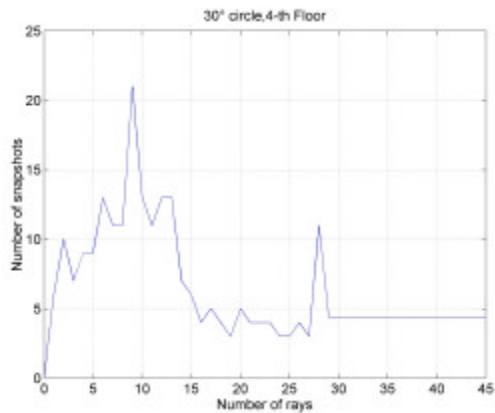


Figure 5. Number of snapshots with a given number of rays inside the dynamic range. The values for a number of rays greater than 29 have been extrapolated. Measurements on the fourth floor.

Though at first glance, the power cdfs might seem Gaussian, we can check that this is not the case by looking at the pdfs in Figure 11. The tails at low powers are longer than the tails at high powers. This is because the high power values are

mainly produced by direct rays, whereas the low power values are mainly produced by reflected rays.

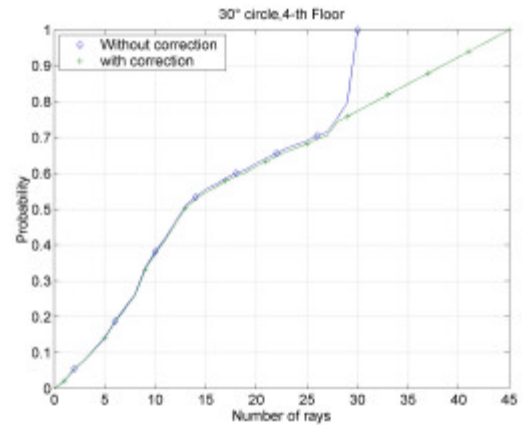


Figure 6. Estimated and corrected cumulative distribution functions (cdfs) for the 30° circular flight on the 4th floor.

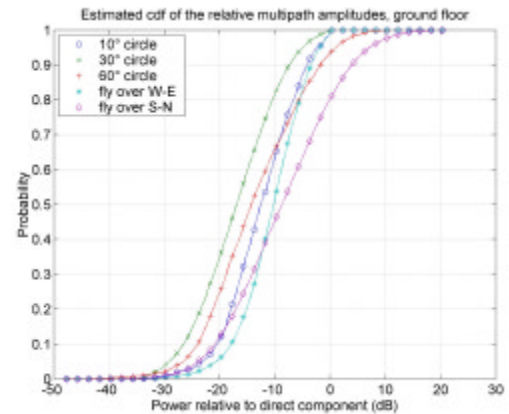


Figure 7. Estimated cdfs of the relative amplitudes of the reflected rays on the ground floor.

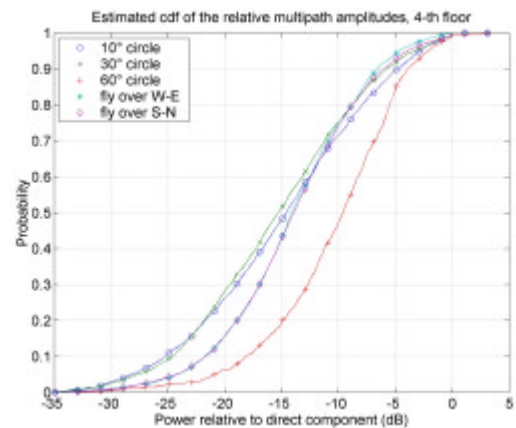


Figure 8. Estimated cdfs of the relative amplitudes of the reflected rays on the fourth floor.

Figures 12-14 plot the cdfs of the reflected ray delays on all three floors. On the ground floor there is a higher density of reflected rays with large delay for the 60° circular flight than for the 10° and 30° circular flights. The measurements on the

fourth and sixth floor have a “step” in the cdfs due to the presence of rays from outside the building (Figure 13). We can see that there are not reflected rays from outside the building for low elevations (10° and 30° circles).

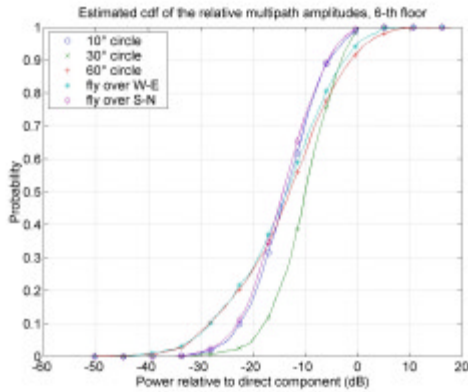


Figure 9. Estimated cdfs of the relative amplitudes of the reflected rays on the sixth floor.

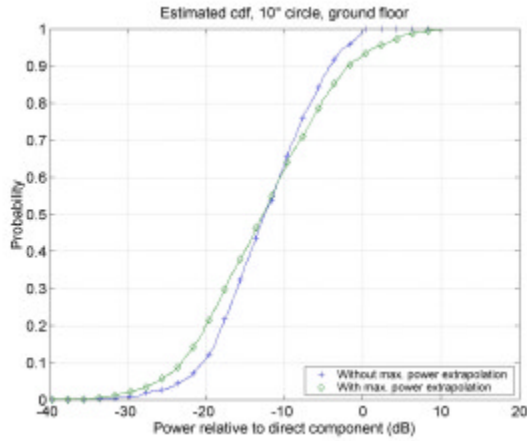


Figure 10. Estimated cdfs without and with maximum power extrapolation.

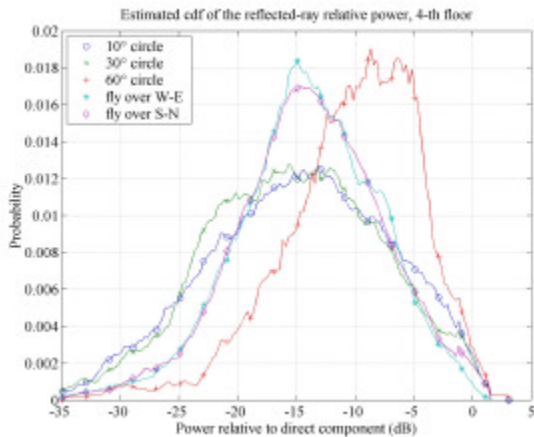


Figure 11. Estimated pdfs of the relative amplitudes of the reflected rays on the fourth floor.

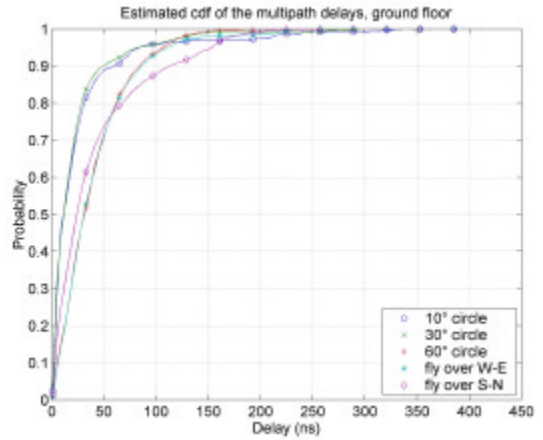


Figure 22. cdf of the delays of the reflected rays on the ground floor.

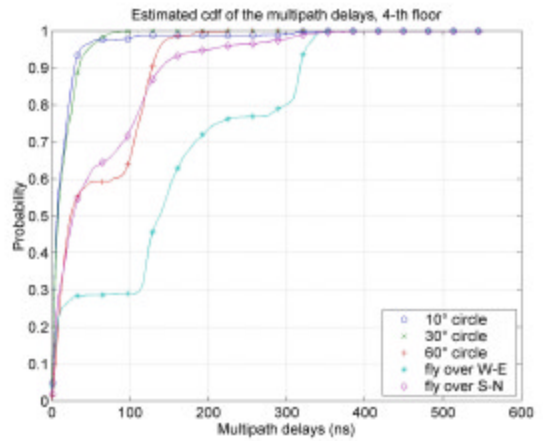


Figure 13. cdf of the multipath delays on the fourth floor.

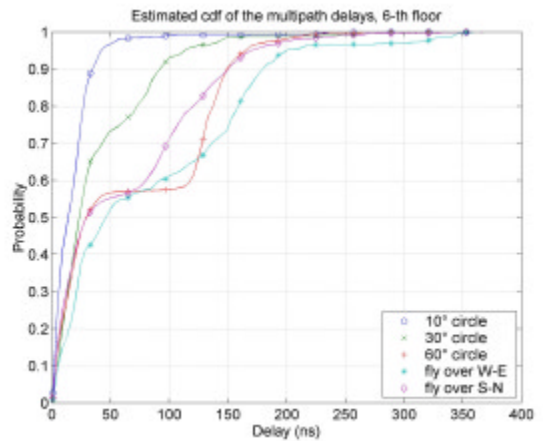


Figure 14. cdf of the delays of the reflected rays on the sixth floor.

Figures 15-19 show sequences of measured PDPs for the various measurement paths.

The estimated cdfs are the reference data for the trial

generators developed. Figure 20 shows the block diagram of the trial generator.

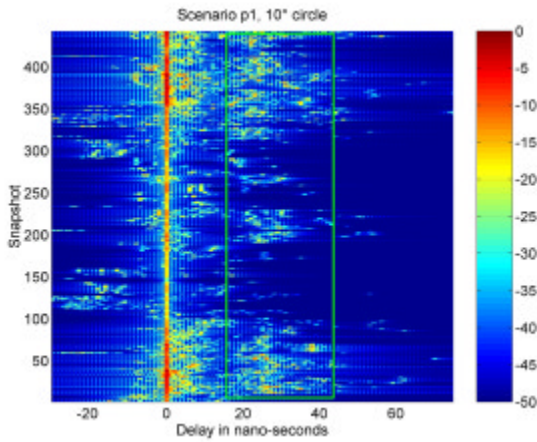


Figure 15. Impulse responses on the sixth floor for the 10° circular flight. The green rectangle marks up the multipath outside the building.

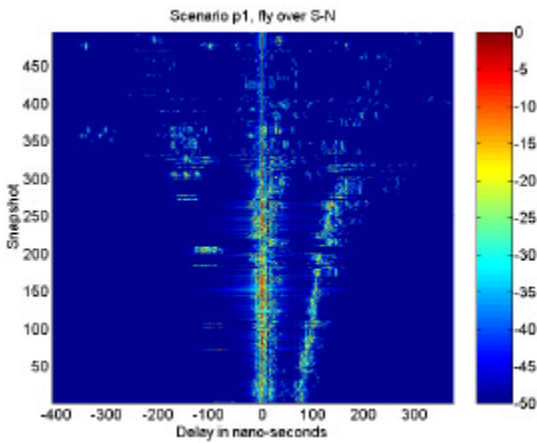


Figure 16. Flight with multipath outside the building, (6<sup>th</sup> floor, South to North flight).

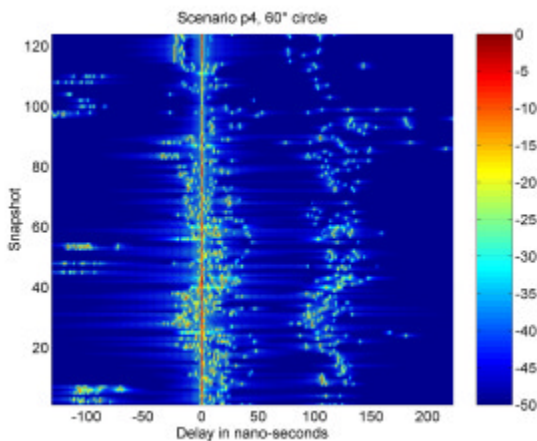


Figure 17. Flight with multipath outside the building, (4<sup>th</sup> floor, South to North flight).

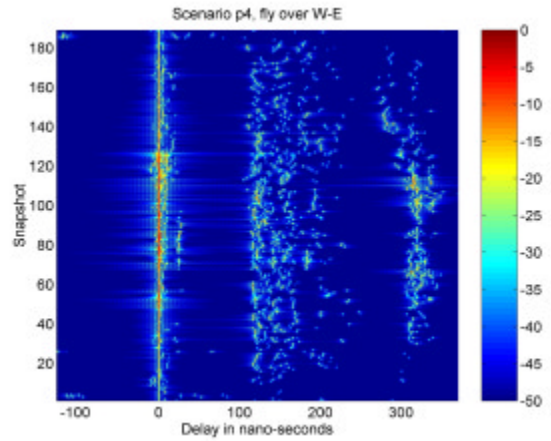


Figure 18. Flight with rays from outside the building, (4<sup>th</sup> floor, West to East flight).

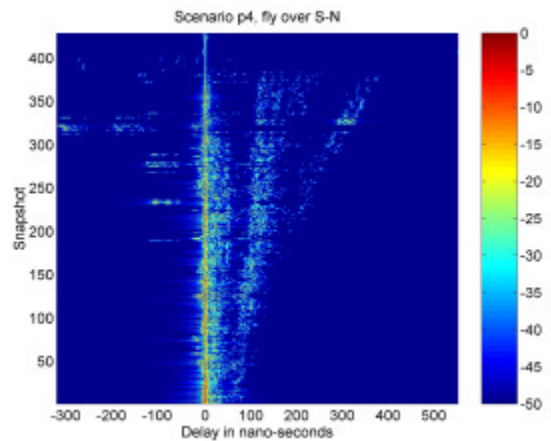


Figure 19. Flight with rays from outside the building, (4<sup>th</sup> floor, South to North flight).

The input parameters to the channel simulator select what measurement is going to be used as a reference. They are,

- Floor 0, 4, 6. (Available floors).
- FlightType '10° circle', '30° circle', '60° circle', 'Flight over W-E', 'Flight over S-N'
- NTrials Number of trials to generate.

The output of the simulator is an array of structures, with each component corresponding to one trial. The structure contains the following fields

- ReflectedRaysDelays Vector of reflected ray delays.
- ReflectedRaysAmplitudes Vector of reflected ray amplitudes.
- DirectRayAmplitude Amplitude of the direct ray. It has been normalised to one, i.e., it contains only the phase.

## DETERMINISTIC CHANNEL MODELING

A deterministic model allows the user to describe in detail the propagation environment and its boundary conditions. The main advantage of this approach in comparison with other approaches, i.e., statistical or empirical, is that it is able to provide a detailed description of the various propagation mechanisms involved since the different multipath contributions reaching the receive antenna are identified and their magnitudes, phases, delays and directions of arrival (DoA) are calculated.

One further relevant advantage of this modeling approach is that, once the model is appropriately fine-tuned after comparison with measurements, it is possible to use this technique and repeatedly apply it to a large number of scenarios so that parameters may be extracted and fed to statistical models which are more convenient for carrying out system-level studies. This procedure was followed later in the development of a statistical channel model.

A ray-tracing approach was chosen as the solution to the channel modeling problem of interest, i.e., characterization of the multipath structure of the received signal in the satellite-to-indoor channels. The work performed also dealt with the aeronautical channel (work presented on an accompanying paper). Several of the developed software modules are common to the study of the two mentioned channels.

Ray-tracing results are then fed to a PO (Physical Optics) electromagnetic (EM) model for the aeronautical channel and to a UGTD (Uniform Geometrical Theory of Diffraction) electromagnetic model for the satellite-to-indoor channel to complete the study. The main modeling steps covered in the simulator implementation are:

- scenario description,
- ray-tracing and polarization-tracking,
- electromagnetic modeling,
- generation of results and
- model validation and fine-tuning.

Next, an outline of the overall process is given. The propagation environment can be described in terms of **flat facets** of different sizes. Environment data for a number of cities, airports, single buildings, airplanes, etc. can be found in standard CAD/virtual reality file formats such as DXF, IGS, VRML, etc. In other cases, CAD modeling tools (e.g. AutoCAD) can be used to generate, in a convenient way, computer descriptions of the modeling scenarios.

The modeling of the environment does not deal with geometrical issues only. Material characterization for each facet included in the environment files must be characterized

from the electromagnetic point of view by means of its constants:  $\epsilon$ ,  $\mu$ ,  $\sigma$ . Once a **standard CAD file** is ready for a given environment, it may be translated into an **internal format** to the propagation modeling tool using very simple **translation routines**. After this, **ray-tracing** and **polarization-tracking** techniques may be used to find what possible multipath contributions are present at the receive antenna.

The EM approach proposed for the modeling of the satellite-to-indoor paths is based on UGTD (Uniform Geometrical Theory of Diffraction) [1-4] techniques applied to plates and wedges with flat facets and straight edges. Ray-tracing is, hence, applied to a scenario made up of flat plates and wedges. For such scenarios it is possible to identify three basic types of rays in addition to the direct ray (Dir):

- reflected rays (R),
- diffracted rays (D) and
- transmitted rays (T).

Further to these basic ray types, **multiple** rays can also be traced: double, triple, ... reflections, diffractions and transmissions. Also **multiple combined (mixed)** rays can be traced, e.g., RD, DR, RDR, TR, TRR, ...

Before proceeding on to the actual electromagnetic modeling stage, a **polarization-tracking** study has to be performed. For each interaction, local coordinate systems must be identified to define both the parallel ( $\parallel$ ) and perpendicular ( $\perp$ ) vectors starting off from the transmit antenna polarization vector (circularly polarized), i.e., its  $\hat{\rho}$  and  $\hat{\phi}$  components, and proceed through the various interactions up to the receive antenna. Assuming that a RHCP signal is transmitted, each contribution reaching the receiver will be depolarized and will, in general, consist of both RHCP and LHCP components (Figure 21).

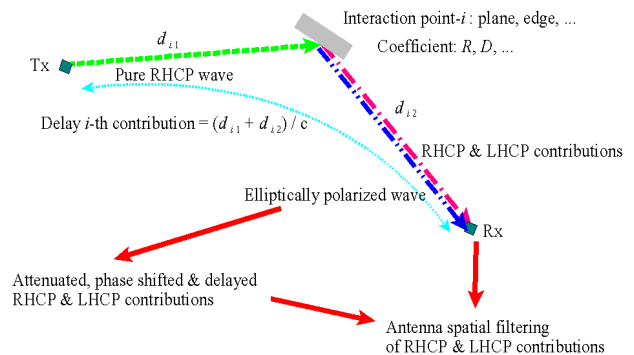


Figure 21. Polarization processing.

The actual **EM modeling** stage is then carried out taking into account the general representation of a ray, i.e.,

$$\vec{E}_{R,D,T} = \vec{E}(p) e^{jF(p)} C A(\rho_1, \rho_2, s) e^{-jks}$$

where

$E(p) e^{jF(p)}$  is the incident field, module and phase, on interaction point  $p$ ,

$C$  is a coefficient representing the type of interaction: reflection, diffraction, transmission,

$A(\varphi_1, \varphi_2, s) = \sqrt{\frac{\varphi_1 \varphi_2}{(\varphi_1 + s)(\varphi_2 + s)}}$  is an spreading factor and

$e^{-jks}$  is a phase term due to the traveled propagation distance,  $s$ , from  $p$  to the receiver.

This step provides information on the amplitudes and phases for both polarizations for the rays traced in previous steps, which already provided information on delay and angle of arrival.

Finally, the **results module** carries out some simple calculations such as receive antenna spatial filtering, etc. to produce the needed results, i.e., a **sequence** of scattering matrices made up of delta functions, two for each traced contributions (RHCP and LHCP or CPOL and XPOL) including information of amplitude, phase, delay and angle of arrival.

The simulation tool is further complemented with a **sequencing module** capable of defining **transmitter / receiver sampling points**. For the satellite-to-indoor channel, the tool is able to accept as an input a sequence of transmitter points, helicopter positions representing a flight around the test building.

The propagation environment was described in a simplified way for the application of deterministic propagation models. To achieve this, only the most significant features, i.e., the larger ones, were included in the input files. The approach was to describe the propagation environment in terms of flat plates. These plates should, in principle, be sufficiently large so that the application of the propagation approach, UTD, is possible/valid. UTD techniques were used on flat plates and straight edges (wedges). This approach is valid for propagation scenarios involving buildings, which can be described in terms of large plates.

Figures 22 and 23 show two AutoCAD views of the test building. In Figure 23 the rays traced for a given receiver locations are also shown.

The use of available commercial products, more specifically AutoCAD, was selected to generate the building environments to be used in the model validation and fine-tuning tasks. Resulting propagation scenario files in .DXF format were translated into the **internal format** used by the propagation-modeling tool. Both, the .DXF and the internal format, are ASCII text files so that they can also be easily read using text editors.

The application of UTD techniques requires prior identification of all possible ray trajectories from the transmitter to the receiver. This involves the application of a number of tracing laws for the various mechanisms involved and the verification of the existence of such rays by checking whether they are obstructed or not. Once all possible ray trajectories have been identified polarization effects must be accounted for. Circular polarization was used in this study; this polarization can be broken down into its two spherical coordinate system components,  $\hat{\theta}$  and  $\hat{\phi}$ . For each interaction with the propagation environment, reflection, diffraction, transmission, the incoming field may also be broken down into its parallel and perpendicular components for which R, D and T coefficients are available. Finally, at the receive antenna, a projection of the electric field onto its local coordinate system is needed. These operations which are called here **polarization tracking** are also carried out before proceeding on to carry out the actual EM calculations.

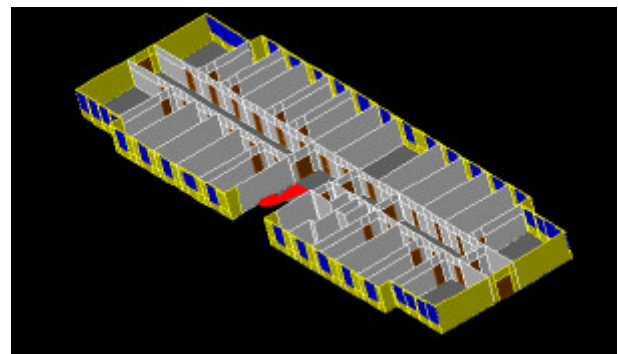


Figure 22. Example of one test building floor in AutoCAD.

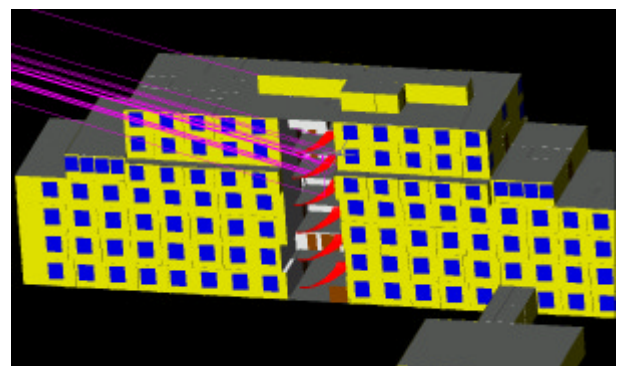


Figure 23. Example of the test building AutoCAD and traced rays.

The three types of basic contributions sought, R, D and T, correspond to different propagation mechanisms that can be described in terms of the Snell's law for reflections, the Keller's law for diffraction (Figure 24) and the Snell's law for refractions (transmissions) (Figure 25).

Snell's law of reflection states that  $\theta_i = \theta_r$ , while Snell's law

of refraction states that

$$\frac{\sin \theta_i}{\sin \theta_r} = \sqrt{\frac{\epsilon_2 \mu_2}{\epsilon_1 \mu_1}} = \frac{n_2}{n_1}$$

where  $n_1$  and  $n_2$  are the refractive indexes for both media. The refractive index of a medium is the ratio of the free space velocity,  $c$ , to the phase velocity in the medium, i.e.,

$$n = \frac{c}{v} = \sqrt{\frac{\epsilon \mu}{\epsilon_0 \mu_0}} = \sqrt{\epsilon_r \mu_r}$$

Moreover, Snell's law states that the incident ray, the normal vector to the interface at the refraction point, and the refracted ray are in the same plane.

In the context of outdoor propagation, the influence of the transmitted rays is very low. When a ray is transmitted through an external building wall, it is rapidly attenuated due to the subsequent obstacles that it encounters after the transmission. The building walls have a finite width such that when a ray is transmitted through a wall.

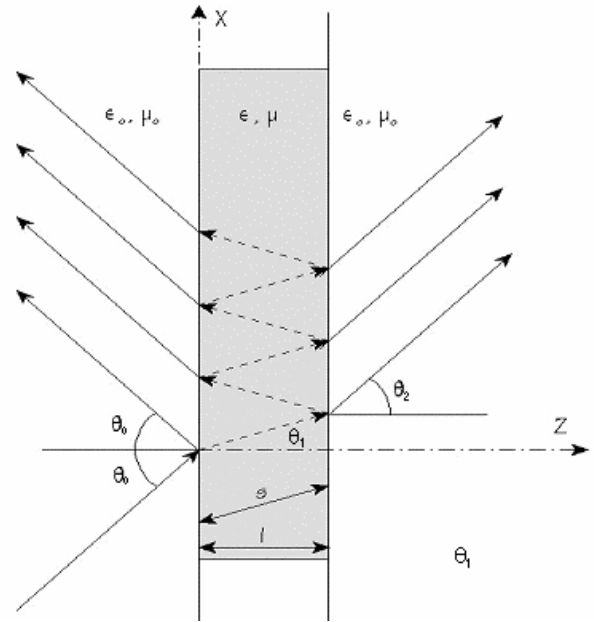


Figure 25. Transmission through walls [3].

Equating both expressions, yields  $\theta_0 = \theta_2$ , which means that the transmitted ray exiting the wall on the other side is parallel to the incoming ray.

As for the diffraction law or Keller's law, it states that a ray obliquely incident on the edge of an obstacle, with an angle  $\beta$ , defines a cone, with angle  $\beta$ , of possible diffracted points as illustrated in Figure 24. The diffracted rays propagate from the diffraction point to the observation point satisfy

$$\hat{s} \cdot \hat{e} = \hat{s}' \cdot \hat{e}$$

where  $\hat{s}'$  is the unit vector in the incident ray,  $\hat{s}$  is the unit vector in the diffracted ray and  $\hat{e}$  is the vector along the edge.

The ray tracing tool implements the following ray and ray combination types:

- R, RR, RRR.
- D, DD.
- RD, DR.
- RRD, DRR, RDR.

In addition to the rays of the above types, it is possible to trace the same rays but including any number of **transmissions**.

Prior to ray-tracing, **acceleration techniques** may be applied [2]. Such techniques are important when the scenarios under analysis are large, i.e., cities, and when the number of simulation points is also large, i.e., test routes sampled with a spacing of the order of the wavelength. Acceleration techniques are also needed when the dynamic range of the

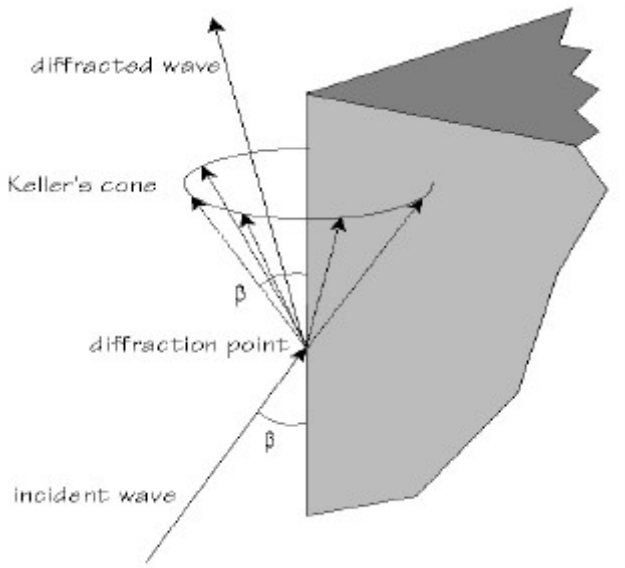


Figure 24. Diffraction law. Keller's cone of diffraction.

The following assumptions have been made with regard to transmissions through walls: (a) The wall medium is homogeneous and isotropic. (b) The two interfaces are locally plane at the transmission points. This is a common assumption in the context of a GO (Geometrical Optics) approach. Applying Snell's laws of reflection and transmission, it can be observed how the incidence angle on the first air-wall interface is equal to the exit angle on the second interface, i.e., wall-air. For the first interface (Figure 25),

$$\beta_0 \sin(\theta_0) = \beta \sin(\theta_1)$$

and for the second interface,

$$\beta \sin(\theta_1) = \beta_0 \sin(\theta_2)$$

signal is sufficiently large that higher-order interactions are significant in the overall received signal as it is the case in terrestrial mobile communications. For navigation systems the dynamic range is much smaller and only single and, at most, double interactions are meaningful.

In case no acceleration techniques are employed, a systematic scan of all planes for transmissions and reflections and edges for diffractions is carried out. This is so for first-order interactions. For second order interactions nested scans (nested "for" loops) are needed, and so on for higher-order interactions.

To carry out the analysis and comparison between measurements and simulations, a section of the helicopter flights around the Joanneum Research building was selected. This section corresponds to flight angles for which the helicopter was in line-of-sight, LOS, or partial LOS conditions with respect to the receiver. The only obstacle was the staircase situated between the wide panel window looking out to the outside of the building, this is illustrated in Figure 26.

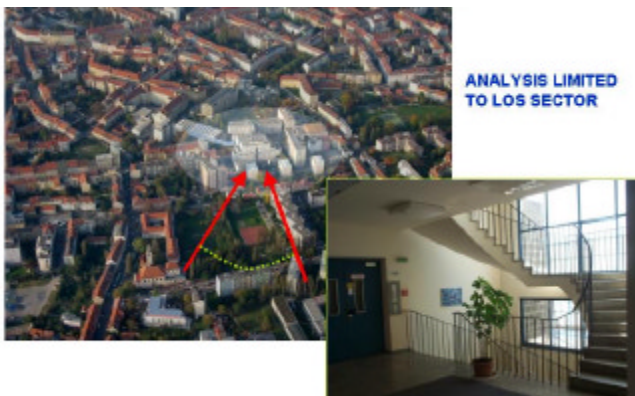


Figure 26. View of the measurement location inside the Joanneum Research building.

The simulations carried out reproduce the measurement conditions, i.e., the receiver was located on the 4th floor of the Joanneum Research building, the transmitter was located on a helicopter and the link elevation angle was on the order of 30° elevation. Twelve measurement points were available corresponding to the LOS section of the flight as mentioned above. Thus twelve simulation points were set in order to perform the validation of the model.

One of the conclusions that can be drawn from first observation of the measured and simulated data is that the paths with delays up to 20 ns correspond to interactions occurring directly within the building. Paths with longer delays are assumed to originate at scattering points outside the building, which have not been considered in the simulation scenario. Thus, even though the actual channel

includes these long-delayed echoes, for validation purposes the comparisons will be limited to this 20 ns delay window. Figure 27. illustrates the distribution of times of arrival in the measured PDPs (power delay profiles).

In the simulations the following ray types were considered: R, RR, D, DD, RD and DR.

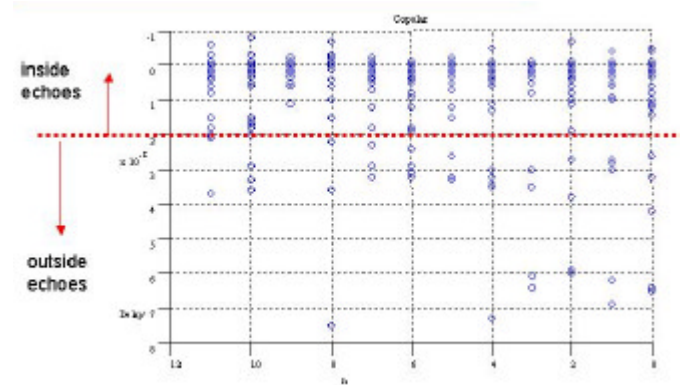


Figure 27. Measured inside-outside echoes.

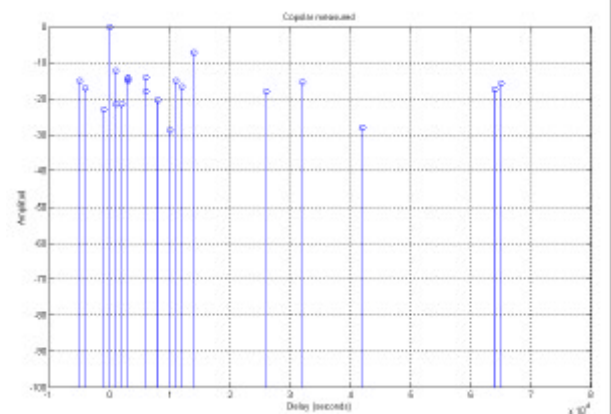


Figure 28. Measured Power Delay Profile for flight point 1.

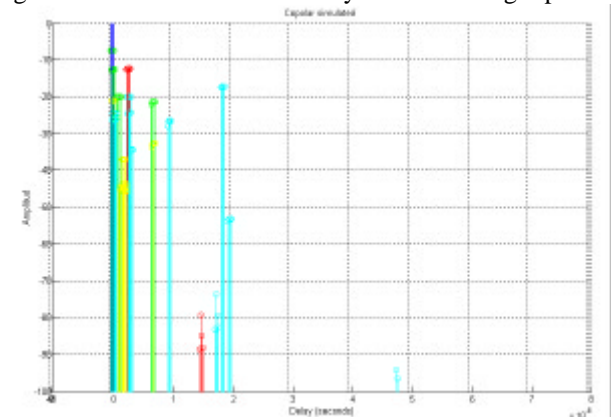


Figure 29. Simulated Power Delay Profile for flight point 1.

It can be observed how first and second order diffractions produced on the spiral staircase contribute an important share of the overall received power found in the simulations given that they show significant dB levels in comparison to some of

the reflected rays and their delays fit in the 20 ns window mentioned above. In Figures 28 and 29 one example of measured and simulated PDPs is given.

The mean excess delay and RMS delay spread are two useful parameters. These values are measures of the severity of a multipath environment. For a given set of multipath signal powers,  $P_i$  and corresponding delays,  $\tau_i$ , the mean and RMS excess delays are calculated as:

$$D = \frac{\sum_i \tau_i P_i}{\sum_i P_i} \quad \text{and} \quad S = \sqrt{\sum_i \tau_i^2 P_i - D^2}.$$

One final parameter of interest can be the Rice factor or carrier-to-multipath ratio, defined for LOS conditions as

$$K(\text{dB}) = 10 \cdot \log_{10}(\sum_i P_i).$$

Table 2 shows a comparison between measured and simulated results. A fairly good agreement was found between the measured and simulated parameters. Similarly, the measured and simulated PDPs also show good similarities. Table 3 shows the list of materials used in the simulations.

Table 2. Measured and simulated values of parameters  $D$ ,  $S$ ,  $K$  for the twelve measurement points.

Profile #	$D_{\text{MEASURED}}$	$D_{\text{SIMULATED}}$	$S_{\text{MEASURED}}$	$S_{\text{SIMULATED}}$	$K_{\text{MEASURED}}$	$K_{\text{SIMULATED}}$
1	8.37 ns	1.77 ns	5.32 ns	4.21 ns	3.1 dB	4.41 dB
2	3.2 ns	2.67 ns	1.60 ns	5.55 ns	0.4 dB	4.38 dB
3	6.06 ns	0.93 ns	5.68 ns	1.40 ns	-0.31 dB	5.69 dB
4	2.79 ns	1.04 ns	2.12 ns	1.39 ns	-4.5 dB	5.72 dB
5	3.45 ns	1.17 ns	2.11 ns	1.35 ns	-1.78 dB	6.71 dB
6	1.86 ns	1.21 ns	1.25 ns	1.33 ns	1.97 dB	6.84 dB
7	3.74 ns	1.31 ns	2.54 ns	1.29 ns	0.03 dB	7.43 dB
8	7.02 ns	1.22 ns	5.84 ns	1.26 ns	5.0 dB	7.04 dB
9	5.15 ns	1.33 ns	3.23 ns	1.27 ns	2.9 dB	7.85 dB
10	2.01 ns	1.29 ns	2.41 ns	1.29 ns	-2.59 dB	7.86 dB
11	8.53 ns	1.18 ns	6.45 ns	1.33 ns	7.11 dB	7.46 dB
12	7.63 ns	1.13 ns	6.64 ns	1.33 ns	4.79 dB	7.29 dB

Table 3. Properties considered for the various materials in the simulation scenario.

Material	$\epsilon_r$	$\sigma$ (S/m)	Thickness
Doors	5.8	0.05-0.06	4 cm
Internal Walls	2.9	0.15-0.16	10 cm
Partitions btwn floors	2.9	0.15-0.16	17-20 cm
External Walls	6	0.001	25-30 cm
Windows	6	0.34-0.35	1 cm
Stairs	5	0.19-0.20	10 cm

## CONCLUSIONS

In this paper, we have presented the analysis of satellite-to-indoor channel measurements. In the case of non line-of-sight propagation, we have analyzed the probability of a reflected ray falling below a given threshold (15 dB and 25 dB) relative to the LOS level. In the case of LOS propagation, we have presented the cdfs of the number of rays, and of their amplitudes and delays. The results show that it is unlikely to have out-of-building rays at low elevations.

For the LOS case, we have developed a statistical model in which the rays in one impulse response are modeled independently with random amplitudes and delays. Finally, we have presented a generator of random impulse response trials that implements this model, and whose input data are the cdfs estimated from the measurements.

Through deterministic, ray-tracing based modeling, it has been confirmed that wall attenuation is the main propagation element, which drastically reduces in-building coverage. This coverage is limited, except for very rare cases, to rooms with external walls. For these external wall rooms and hallways it has been found that accounting for diffracted rays helps improve the predictions based only on reflected rays. In this way, a larger number of rays are traced that match more closely the distribution of rays and the power balance in the measurements.

## ACKNOWLEDGEMENTS

The work presented in this paper was carried out under an European Space Agency, ESA, contract entitled "Navigation signal measurement campaign for critical environments", carried out by JOANNEUM RESEARCH (Austria) with subcontracts to DLR (Germany) and the University of Vigo (Spain), are presented.

## REFERENCES

- [1] R.G.Kouyoumjian and P.H.Pathak  
A uniform geometrical theory of diffraction for an edge in a perfectly conducting surface.  
Proc. IEEE, Vol 62, pp. 1448-1461, 1974
- [2] F. Aguado, A. Formella; J.M.Hernando, F.Isasi and F. Perez Fontan. Efficient ray-tracing acceleration techniques for radio propagation modeling. IEEE Transactions on Vehicular Tech., Vol. 49, No. 6, Nov. 2000, pp. 2089 -2104
- [3] I. de Coster. Deterministic propagation prediction for wireless communication systems  
PhD Thesis. Katholieke Universiteit Leuven, 2000.
- [4] G. A. J. van Dooren. A deterministic approach to the modeling of electromagnetic wave propagation in urban environments. PhD Thesis, 1994. TUE, Eindhoven.

Table 1. Analysis of the measurements without direct ray.

Scenario	Flight type	Probability of being above the 15 dB limit ( $\text{Prob}_{15}$ )	Probability of being above the 25 dB limit ( $\text{Prob}_{25}$ )	Flight Max. Power to Flight Average Max. power ratio (S, dB)	Presence of direct signal on the whole flight	Multipath outside the building
Ground floor (P5)	10° circle	0.16935	0.73387	10.493	Yes	No
	30° circle	0.10732	0.57073	9.3752	Yes	No
	60° circle	0.29397	0.8973	8.5406	No	No
	Fly over S-N	0.15	0.65	10.208	Yes	No
	Fly over W-E	0.31847	0.89809	8.6302	No	No
	People moving in lobby	0.23691	0.78512	5.8167	No	No
Fourth floor (P4)	10° circle	0.17073	0.66341	9.4418	Yes	No
	30° circle	0.097701	0.48851	9.3547	Yes	No
	60° circle	0.46185	0.95582	6.3781	No	Yes
	Fly over S-N	0.19919	0.77658	6.3077	Yes	Yes
	Fly over W-E	0.26836	0.84266	5.2459	Yes	Yes
Sixth floor (P1)	10° circle	0.26243	0.73757	8.0616	Yes	Yes
	30° circle	0.38247	0.94024	8.3649	No	No
	60° circle	0.011931	0.26547	16.057	No	No
	Fly over S-N	0.076372	0.62053	8.3359	Yes	Yes
	Fly over W-E	0.51515	0.98485	6.6219	No	No

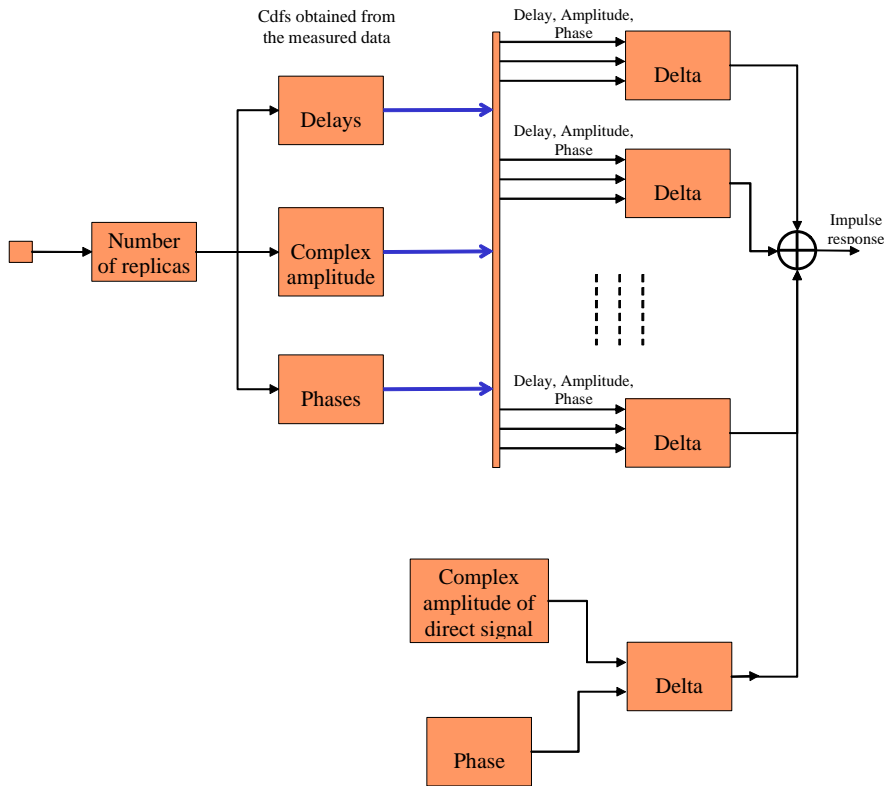


Figure 20. Block diagram of the trial generator.